Optics Letters

# Vector flow velocity measurement based on bidirectional scanning in optical coherence tomography

Yun Tang,[1,2] Sijie Xiong,[3] Lu Yang,[1] Bingyan Zhang,[1] Changyong Chen,[1] Cui Ma,[1] Zhiyi Liu,[1] and Zhihua Ding[1,2,*]

[1]State Key Laboratory of Extreme Photonics and Instrumentation, College of Optical Science and Engineering, Zhejiang University, Hangzhou 310027, China
[2]ZJU-Hangzhou Global Scientific and Technological Innovation Center, Zhejiang University, Hangzhou 311215, China
[3]State Key Laboratory of Advanced Drug Delivery and Release Systems, College of Pharmaceutical Sciences, Zhejiang University, Hangzhou 310058, China
*zh_ding@zju.edu.cn

Received 2 October 2025; revised 31 October 2025; accepted 6 November 2025; posted 17 November 2025; published 10 December 2025

**We propose to measure the vector velocity of the flow field based on bidirectional scanning in optical coherence tomography (OCT). Transverse velocity was determined by dynamic light scattering OCT (DLS-OCT) under four introduced transverse synthetic speeds, while axial velocity was obtained by Doppler OCT (DOCT). The flow fields within two straight channels and an improperly welded Y-junction were measured. *In vivo* measurement on a rabbit was further conducted. Without resorting to system modification and requiring only four scan biases, the proposed method is advantageous in measurement of the vector velocities of a complex flow field.** 

https://doi.org/10.1364/OL.580963

Many basic research and biomedical applications require the measurement of vector flow velocities to characterize the complex flow fields and elucidate the physiological and pathological mechanisms associated with flow dynamics [1–3]. Optical methods such as laser Doppler flowmetry (LDF) [4], laser speckle velocimetry (LSV) [5], and particle image velocimetry (PIV) [6] are widely used because of their high spatiotemporal resolutions and non-contact characteristics. However, due to a lack of depth-resolved capability, their applications in the deep regions are usually limited. Optical coherence tomography (OCT), which uses low-coherence interferometry to obtain depth-resolved signals within a depth range of 1–3 mm, has already played an important role in hemodynamic research [7–9]. The OCT-based methods for quantification of flow field are mainly divided into Doppler OCT (DOCT) [10] and dynamic light scattering OCT (DLS-OCT) [11]. The measurements provided by DOCT rely on the Doppler angle and lack sensitivity to the flow orthogonal to the detection beam. To realize the determination of the vector velocity, multi-beam ODT was proposed, where the illumination/detection configuration was modified to be a complex one [12,13]. On the other hand, a quantitative model for DLS-OCT was first developed and applied to measure both longitudinal and transverse flow speeds, although the directions of the flow fields were not resolved [14]. To resolve directional ambiguity of the transverse flow, lateral scanning was first introduced to DLS-OCT, where the method based on the minimum decay rate was suggested [15]. However, this method requires a series of scan biases to find a point at which the scan bias best matches the fluid flow.

In this paper, we propose to measure the transverse velocity using only four scan biases along orthogonal axes of the transverse plane in OCT. The proposed method does not require modification of the system configuration and needs only four scan biases. Therefore, it has the advantages of system simplicity and measurement speediness.

Figure 1 demonstrates the schematic of the proposed method. The layout of the flow field and the illumination beam under both forward scanning (FS) and backward scanning (BS) controlled by the galvanometer in the sample arm is shown in Fig. 1(a). The vector velocity $\vec{v_f}$ with a longitudinal angle of $\gamma$ and a latitudinal angle of $\theta$ in the Cartesian coordinate system shown in Fig. 1(b) can be decomposed into the transverse velocity $\vec{v_t}$ and the axial velocity $\vec{v_z}$. Based on the transverse velocities ($\vec{v_s}$, $-\vec{v_s}$) introduced by both FS and BS along the X axis, and utilizing the parallelogram rule ($\vec{v_{l1}} = \vec{v_t} - \vec{v_s}$, $\vec{v_{l2}} = \vec{v_t} + \vec{v_s}$) shown in Fig. 1(c), two candidate transverse vector velocities $\vec{v_t}$ ($v_t$, $\gamma$) are founded to be qualified by two transverse synthetic speeds ($|\vec{v_{l1}}|$, $|\vec{v_{l2}}|$). To resolve the directional ambiguity, additional bidirectional scanning along Y axis is required [Supplement 1]. Then, combined with the axial velocity $\vec{v_z}$ obtained by the phase-resolved DOCT approach [10], the vector velocity $\vec{v_f}$ is thus determined.

The depth ($z$) dependent first-order normalized autocovariance function of the complex OCT signal can be expressed by [16,17]:

$$C_1(z,\tau) = e^{i2nk_0 v_z(z)\tau} e^{-4n^2 {k_0}^2 D\tau} e^{-\left(\frac{v_t(z)^2}{w_l^2}\right)\tau^2} e^{-\left(\frac{v_z(z)^2}{2w_z^2}\right)\tau^2}, \quad (1)$$

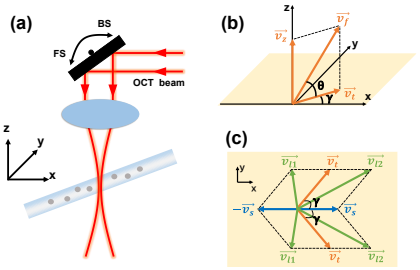


**Fig. 1.** Determination of the transverse velocity by bidirectional scanning. (a) The layout of the flow field and the illumination beam under FS and BS. (b) Orientation angles and two decomposed components of the velocity vector. (c) Parallelogram rule for four transverse synthetic speeds at the transverse plane.

where $n$ is the refractive index of the medium of the flow field, $k_0$ is the center wavenumber, $D$ is the diffusion coefficient of the flow field, $\tau$ is the time lag, $w_l$ is the beam waist under the assumption of a Gaussian distribution of the illumination beam, and $w_z$ is the coherence length waist. Eq. (1) is valid assuming that the average number of particles in the scattering volume, N, is sufficiently large (typically N ≥ 100) [17]. To determine the axial velocity $\overrightarrow{v_z}$, the phase information of the first term in Eq. (1) was exploited [Supplement 1]. To determine the transverse velocity $\overrightarrow{v_t}$ ($v_t$, $\gamma$), instead of using Eq. (1), the second-order normalized autocovariance of the intensity signals $C_2(z,\tau)$ was adopted, which avoids the operation of complex numbers for faster computation [Supplement 1]. Based on the Siegert relationship, the normalized second-order mean-subtracted intensity autocovariance function is given by [16]:

$$C_2(z,\tau) = e^{-8n^2{k_0}^2 D\tau}\, e^{-\left(\frac{2v_t(z)^2}{w_l^2}\right)\tau^2}\, e^{-\left(\frac{v_z(z)^2}{w_z^2}\right)\tau^2}. \quad (2)$$

Caution must be taken in extremely dilute samples and/or very small scattering volumes, where the assumption of sufficiently large N for Eq. (1) no longer holds, and an additional number fluctuation term should be included in Eq. (2) [18]. To be concise, replace the quadratic term in Eq. (2) with $\eta$ and let $-\frac{2}{w_l^2} = b$, $-\frac{1}{w_z^2} = c$, then we get:

$$\eta = b{v_t(z)}^2 + c{v_z(z)}^2. \quad (3)$$

Obviously, $v_t(z)$ and $v_t(z)$ are inseparable in Eq. (2), although this quadratic term $\eta$ can be decoupled from the linear term associated with $D$. To determine both $v_t$ and $\gamma$ for $\overrightarrow{v_t}$, positive and negative biased velocities were introduced by both FS and BS. Without loss of generality, one set of bidirectional scanning was set along the X axis. Correspondingly, the quadratic terms for both cases of FS and BS are modified to be:

$$\eta_{FS}(z) = b\left({v_t(z)}^2 - 2v_t(z)\, v_s \cos\gamma(z) + v_s^2\right) + c{v_z(z)}^2, \quad (4)$$

$$\eta_{BS}(z) = b\left({v_t(z)}^2 + 2v_{t(z)} v_s \cos\gamma(z) + v_s^2\right) + c{v_z(z)}^2, \quad (5)$$

Then $\overrightarrow{v_t}$ ($v_t$, $\gamma$) is determined by:

$$v_{t(z)} = \sqrt{\frac{\eta_{FS}(z) + \eta_{BS}(z) - 2bv_s^2 - 2c{v_z(z)}^2}{2b}}, \quad (6)$$

$$\gamma(z) = \cos^{-1} \times \left(\frac{\eta_{FS}(z) - \eta_{BS}(z)}{2\sqrt{2}v_s} \frac{1}{\sqrt{b\left(\eta_{FS}(z) + \eta_{BS}(z) - 2bv_s^2 - 2c{v_z(z)}^2\right)}}\right), \quad (7)$$

where $\eta_{FS}$, $\eta_{BS}$ are the fitted quadratic terms of the normalized second-order mean-subtracted intensity autocovariance functions for both cases of FS and BS, $b$ and $c$ are calculated from the calibrated $w_l$ and $w_z$. The determined $\gamma(z)$ using Eq. (7) is in the range (0, π), while it should span over the range (0, 2π). To resolve the complete vector direction, an additional set of FS and BS along the Y axis was performed [Supplement 1].

The established spectral-domain OCT (SD-OCT) system operated at an A-line rate of 100 kHz [19] was used to fetch the OCT signals from the flow field. The light source implemented in the system has a center wavelength of 840 nm with a FWMH bandwidth of 47 nm, and the coherence length waist $w_z$ was calibrated to be 6.2 μm. Triangular waves were applied to the galvanometer to realize bidirectional scanning. To avoid nonlinear scanning and hysteresis between FS and BS, A-lines corresponding to the central part of the lateral length were sampled for subsequent processing. The position errors in lateral scanning were much smaller than the beam waist $w_l$ and can be neglected in this study. To make the flow field detectable by the SD-OCT system, the aqueous solution made by monodisperse polystyrene microspheres (diameter: 100 nm, solid content: 2.5%, $n$: 1.6, supplier: Jiangsu Zhichuan Technology, China) was adopted as the scattering medium within the flow field. The beam waist $w_l$ and the linear term $8n^2{k_0}^2 D$ were measured to be 16 μm and 1.24 $\text{ms}^{-1}$, respectively, within the static medium based on the reported method [17]. A syringe pump (TYD02-02, Leadfluid, China) and a 50 mL syringe (BD Plastipak) were used to control the flow speed. To comply with actual application scenarios, the linear term is not treated as a known parameter but fitted simultaneously with the quadratic term. The experimental parameters for data acquisition, if not specified, were set as follows. The normalized second-order mean-subtracted intensity autocovariance functions were averaged over 100 repeats and then used for parameter fitting. The flow speeds were obtained from four repeated measurements and represented by their means and standard deviations. The orientation angles were obtained at the center of the tube by axial averaging among 60 pixels.

To demonstrate the feasibility of the proposed method for the determination of $\overrightarrow{v_t}$ ($v_t$, $\gamma$), the flow fields within two straight channels were measured. Since there is no directional ambiguity in this situation, bidirectional scanning was only conducted along X axis. The first straight channel made of a quartz capillary tube with an inner diameter of 0.5 mm was prepared and placed on the x-y plane with zero latitudinal angle. The channel was oriented at four longitudinal angles ($\gamma 1_{true} = 33°$, $\gamma 2_{true} = 45°$, $\gamma 3_{true} = 62°$, $\gamma 4_{true} = 85°$) and pumped at six volumetric flow rates (Q1 = 0.12 mL/min, Q2 = 0.24 mL/min, Q3 = 0.35 mL/min, Q4 = 0.47 mL/min, Q5 = 0.59 mL/min, Q6 = 0.71 mL/min) corresponding to average flow speeds of 10 mm/s, 20 mm/s, 30 mm/s, 40 mm/s, 50 mm/s, 60 mm/s, respectively. The biased speed $v_s$ was introduced through precise control of the voltage applied to the galvanometer. Under a lateral scanning distance of 1 mm within the data acquisition time of 2500 A-lines, $v_s$ was set to be 40 mm/s for both FS and BS to ensure the fit-

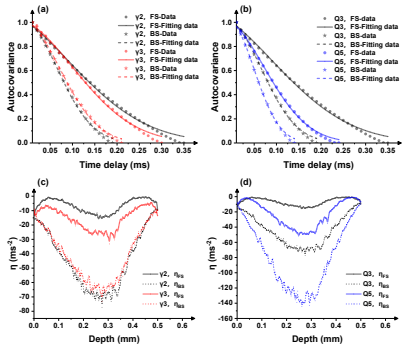


**Fig. 2.** Normalized second-order mean-subtracted autocovariance functions and their fittings at the center of the capillary for (a) two longitudinal angles for both FS and BS under the volumetric flow rate of Q5 and (b) two volumetric flow rates for both FS and BS under the longitudinal angle of $\gamma 2$. Central depth profiles of the quadratic terms for (c) two longitudinal angles under the volumetric flow rate of Q3, and (d) two volumetric flow rates under the longitudinal angle of $\gamma 2$.

ting accuracy [Supplement 1]. Typical normalized second-order mean-subtracted intensity autocovariance functions $C_2$ and their fittings are shown in Figs. 2(a) and 2(b), where the dependence of $C_2$ on the volumetric flow rate, the longitudinal angle, and the scanning direction is demonstrated. Using these fittings of $C_2$, quadratic terms $\eta$ were further fitted through their quadratic dependence on time. Representative central depth profiles of the quadratic terms $\eta_{FS}(z)$, $\eta_{BS}(z)$ are shown in Figs. 2(c) and 2(d), where the dependence of $\eta$ on the volumetric flow rate, the longitudinal angle, and the scanning direction is exhibited. Furthermore, the depth dependence of $\eta$ is observed, which is due to the depth dependence of flow velocity within the capillary tube. Substituting the calibrated and set parameters ($b=-0.0078\,\mu m^{-2}$, $c=-0.026\,\mu m^{-2}$, $v_s=40$ mm/s, $v_z=0$ mm/s) and the fitted quadratic terms ($\eta_{FS}(z)$, $\eta_{BS}(z)$) into Eqs. (6) and (7), both $v_t$ and $\gamma$ for $\vec{v_t}$ were then determined. Figure 3(a) shows the central depth profiles of the measured and the preset flow speeds within the capillary tube under six volumetric flow rates (Q1–Q6), where the channel was oriented on the x-y plane with a fixed longitudinal angle ($\gamma 2_{true}=45°$). The preset velocities were calculated from the pump's flow rate and the inner diameter of the tube using the Poiseuille's law. The speeds at the center of the tube were measured to be approximately twice the average speeds under six volumetric flow rates (Q1–Q6), exhibiting a typical characteristic of Poiseuille parabolic distribution [20]. The measured $\gamma$ under different volumetric flow rates are shown in Table 1. It is observed that the measured errors are somehow dependent on the volumetric flow rates and the angles to be determined. Except for the cases of $\gamma 1_{true}$ under volumetric flow rates of Q1, Q2, Q3, all the measured $\gamma$ are basically in agreement with the set values. The relatively larger errors in measurements for the cases of $\gamma 1_{true}$ under volumetric flow rates of Q1, Q2, Q3 could be attributed to the uncertainty in fitting of $\eta_{FS}$ under a small value [16], since small synthetic speeds resulted. It should be noted that if bidirectional scanning along both the X and Y axes were performed, these errors could be reduced.

To demonstrate the feasibility of the method for the determination of $\vec{v_f}$ ($v_f$, $\gamma$, $\theta$), the second straight channel made of a quartz capillary tube with an inner diameter of 1 mm was pre-

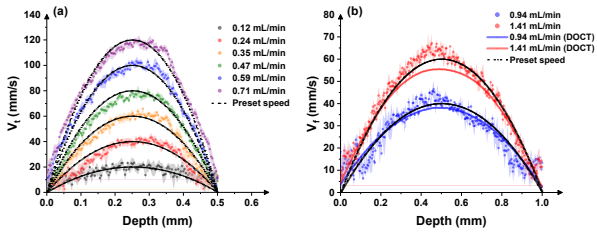


**Fig. 3.** Central depth profiles of the measured flow speeds (mean ± std) and corresponding preset ones within capillary tubes with (a) 0.5 mm inner diameter oriented at (45°, 0°) and (b) 1 mm inner diameter oriented at (45°, 6°).

**Table 1. $\gamma$ Measurements under Six Volumetric Flow Rates**

| Q mL/min | $\gamma 1$ ($\gamma 1_{true}=33°$) | $\gamma 2$ ($\gamma 2_{true}=45°$) | $\gamma 3$ ($\gamma 3_{true}=62°$) | $\gamma 4$ ($\gamma 4_{true}=85°$) |
|---|---|---|---|---|
| 0.12 | 23.6° ± 8.0° | 46.6° ± 7.2° | 65.9° ± 3.4° | 86.1° ± 2.1° |
| 0.24 | 19.1° ± 7.1° | 38.7° ± 5.7° | 60.8° ± 3.0° | 85.1° ± 1.7° |
| 0.35 | 25.3° ± 6.5° | 41.4° ± 3.0° | 61.5° ± 2.7° | 84.5° ± 2.2° |
| 0.47 | 32.7° ± 3.5° | 44.1° ± 2.9° | 61.8° ± 3.3° | 84.0° ± 1.9° |
| 0.59 | 32.6° ± 5.4° | 46.6° ± 3.3° | 63.1° ± 3.2° | 84.8° ± 2.2° |
| 0.71 | 34.7° ± 4.6° | 46.8° ± 3.1° | 63.6° ± 2.9° | 84.2° ± 2.5° |

**Table 2. $\gamma$ and $\theta$ Measurements under Two Volumetric Flow Rates**

| Q mL/min | ($\gamma 2$, $\theta$) ($\gamma 2_{true}=45°$, $\theta_{true}=6°$) | ($\gamma 3$, $\theta$) ($\gamma 3_{true}=62°$, $\theta_{true}=6°$) |
|---|---|---|
| 0.94 | (43.7° ± 4.4°, 5.8° ± 0.3°) | (61.8° ± 4.3°, 6.1° ± 0.4°) |
| 1.41 | (46.3° ± 3.7°, 5.6° ± 0.2°) | (63.0° ± 3.3°, 5.9° ± 0.3°) |

pared and oriented at a non-zero latitudinal angle ($\theta_{true}=6°$). The channel was pumped at 0.94 and 1.41 mL/min with average flow rates of 20 and 30 mm/s. Under a lateral scanning distance of 2 mm within the data acquisition time of 5000 A-lines, $v_s$ remained 40 mm/s for both FS and BS. Figure 3(b) shows the central depth profiles of the measured and the preset flow speeds within the capillary tube with fixed orientation ($\gamma 2_{true}=45°$, $\theta_{true}=6°$) under two volumetric flow rates. Again, the determined speeds at the center are observed to be about twice the average speeds estimated from two volumetric flow rates. In comparison, under the condition of a known Doppler angle, the results obtained by the DOCT method are shown in Fig. 3(b), which are basically consistent with those provided by the proposed method, but there are obvious deviations. These deviations are caused by the following three factors. The first is the Doppler broaden introduced by the longitudinal velocity gradient within the coherent gate. The second is the additional Doppler broaden introduced by fluctuations of the longitudinal flow velocities among the bias scans. The third is that the refraction of the detection beam within the channel was not taken into account. Furthermore, the orientations ($\gamma$, $\theta$) determined under the two volumetric flow rates are shown in Table 2 and are in good agreement with the set values.

To realize a more complex flow field, a Y-junction was welded by a quartz capillary tube with an inner diameter of 2 mm as the main channel and two quartz capillary tubes with inner diameters of 1 and 1.5 mm, respectively, as two branch pipes.

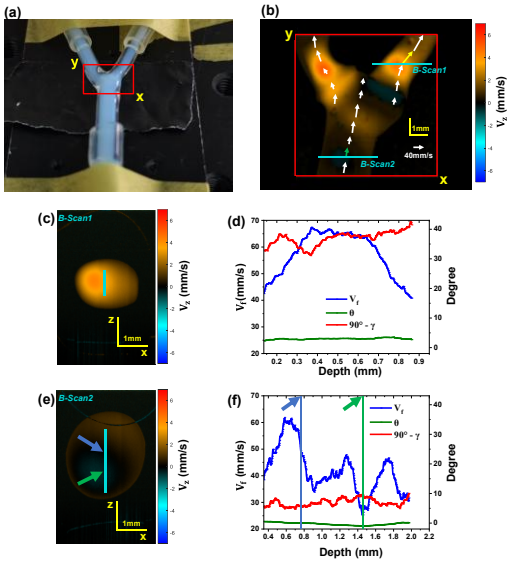


**Fig. 4.** (a) Photo of the Y-junction. (b) DOCT *enface* image revealing $v_z$ distribution and overlaid arrows denoting transverse vector $\vec{v_t}$ at represented positions. (c) DOCT B-scan image at "B-Scan1" of the branch pipe shown in (b). (d) Profiles of $\vec{v_f}$ ($v_f$, $\gamma$, $\theta$) in depth range indicated by the vertical line in (c). (e) DOCT B-scan image at "B-Scan2" of the main channel shown in (b). (f) Profiles of $\vec{v_f}$ ($v_f$, $\gamma$, $\theta$) in depth range indicated by the vertical line shown in (e).

As shown in Fig. 4(a), this Y-junction was fabricated improperly, resulting in its irregular shape, which is conducive to the formation of a more complex flow field. The main channel was pumped at 4 mL/min and the resulted flow field within the Y-junction was measured. $v_s$ was set to 100 mm/s for both FS and BS with a lateral scanning distance of 10 mm corresponding to 10000 A-lines [Supplement 1]. Parameter fitting was performed after averaging the normalized second-order mean-subtracted intensity autocovariance functions among 30 repeats. A typical DOCT *enface* image revealing the $v_z$ distribution of the flow field is shown in Fig. 4(b), where transverse velocities $\vec{v_t}$ at representative positions are also presented by the arrows with assigned lengths ($v_t$) and directions ($\gamma$). Two DOCT B-scan images, one at "B-Scan1" of the branch pipe and the other at "B-Scan2" of the main channel, shown in Fig. 4(b), are given in Figs. 4(c) and 4(e), respectively. The profiles of $\vec{v_f}$ ($v_f$, $\gamma$, $\theta$) of the flow field over the central depth ranges indicated by the vertical lines in Figs. 4(c) and 4(e) are demonstrated in Figs. 4(d) and 4(f), respectively. No repeated measurements were conducted here. As shown in Fig. 4(d), although there are obvious fluctuations in the flow direction ($\gamma$ and $\theta$), the flow speed at "B-Scan1" of the branch pipe maintains the characteristic of Poiseuille parabolic distribution. However, at "B-Scan2" of the main channel, as shown in Fig. 4(f), a complex flow pattern is presented, while the averaged flow speed at "B-Scan2" is about 20 mm/s. To illustrate the characteristics of the resulted complex flow pattern, the velocities at two representative positions marked with blue and green arrows are shown in Figs. 4(e) and 4(f) are selected for further comparison. As shown in Fig. 4(f), at the position indicated by the blue arrow, the determined $\theta$ approaches zero, indicating the flow direction is almost orthogonal to the detection beam. In such a situation, the sensitivity of the velocity measurement provided by the DOCT is the lowest, and a value close to zero was assigned for $v_z$ as shown in Fig. 4(e). In contrast, the developed method offers full information of the flow velocity, and a non-zero value of 48 mm/s for the flow speed was determined at this position, indicated by the blue arrow. In contrast, at the position indicated by the green arrow, the local minimum of the flow speed was measured under a negative $\theta$ with the local maximum absolute value. The alteration of $\theta$ from a positive value to a negative value indicates the direction change along the z-axis, resulting in an obvious change in the flow speed. It is worth noting that the influence of this directional change on the flow speed is much greater than that of the fluctuation of $\gamma$. Pronounced speed fluctuations and directional changes are observed in the measured velocities as shown in Fig. 4(f).

In vivo measurement on a rabbit was further conducted [Supplement 1], demonstrating the capability of the method in real applications.

The limitation of the method is the reduced spatial resolution and time resolution due to the required bias scans as well as sequential samplings, and the balance should be made among spatial resolution, time resolution, and measurement accuracy.

In summary, the method for the determination of the vector flow velocity was established in the SD-OCT system.

**Funding.** National Natural Science Foundation of China (62035011, 62575254, 62275232).

**Disclosures.** The authors declare no conflicts of interest.

**Data availability.** The data that support the findings of this study are available from the corresponding authors upon request.

**Supplemental document.** See Supplement 1 for supporting content.

## REFERENCES

1. B. K. Huang and M. A. Choma, Cell. Mol. Life Sci. **72**, 1095 (2015).
2. L. Qi, J. Zhu, A. M. Hancock, *et al.*, Biomed. Opt. Express **7**, 601 (2016).
3. D. Pinho, V. Carvalho, I. M. Goncalves, *et al.*, J. Pers. Med. **10**, 249 (2020).
4. P. A. Oberg, Crit. Rev. Biomed. Eng. **18**, 125 (1990).
5. M. Qian, J. Liu, M. S. Yan, *et al.*, Opt. Express **14**, 7559 (2006).
6. C. E. Willert and M. Gharib, Exp. Fluids **10**, 181 (1991).
7. P. Mukherjee, S. Fukuda, D. Lukmanto, *et al.*, Sci Rep. **13**, 15324 (2023).
8. J. de Wit, S. Tonn, M. R. Shao, *et al.*, Nat. Commun. **15**, 8353 (2024).
9. Y. Tang, J. Zhu, L. Q. Zhu, *et al.*, Appl. Phys. Lett. **120**, 163702 (2022).
10. R. A. Leitgeb, R. M. Werkmeister, C. Blatter, *et al.*, Prog. Retin. Eye Res. **41**, 26 (2014).
11. J. Lee, W. C. Wu, J. Y. Jiang, *et al.*, Opt. Express **20**, 22262 (2012).
12. C. X. Dai, X. J. Liu, H. F. Zhang, *et al.*, Invest. Ophthalmol. Vis. Sci. **54**, 7998 (2013).
13. R. M. Werkmeister, N. Dragostinoff, M. Pircher, *et al.*, Opt. Lett. **33**, 2967 (2008).
14. N. Weiss, T. G. van Leeuwen, and J. Kalkman, Phys. Rev. E **88**, 042312 (2013).
15. B. K. Huang and M. A. Choma, Opt. Lett. **39**, 521 (2014).
16. N. Weiss, T. G. van Leeuwen, and J. Kalkman, Opt. Express **23**, 3448 (2015).
17. K. Cheishvili and J. Kalkman, Opt. Express **30**, 23382 (2022).
18. T. W. Taylor and C. M. Sorensen, Appl. Optics **25**, 2421 (1986).
19. T. Han, S. H. Qian, J. Meng, *et al.*, Laser Photon. Rev. **19**, 2401479 (2025).
20. J. Pfitzner, Anaesthesia **31**, 273 (1976).